Research Article | Vol. 33, No. 16 / 11 Aug 2025 / Optics Express 34800
Optics EXPRESS

Bendable grating for monochromatization of extreme-ultraviolet light

GABRIELE ZENI,[1,*] FABIO FRASSETTO,[1] PAOLA ZUPPELLA,[1] ANTONIO VANZO,[1,2] STEFANO BONORA,[1] MARCELLO CORENO,[3] AND LUCA POLETTO[1]

[1]CNR-IFN Padova, Via Trasea 7, 35131 Padova, Italy
[2]Department of Information Engineering, University of Padova, Via Gradenigo 6/b, 35131 Padova, Italy
[3]CNR-ISM, Trieste Branch, Strada Statale 14—km 163,5, 34149 Basovizza, Italy
[*]gabriele.zeni@pd.ifn.cnr.it

Abstract: Gratings used in laboratory applications such as compensated and non-compensated monochromators have usually a plane geometry and require additional optical elements, mirrors, to focalize the selected spectral component. An active grating, whose curvature radius can be adjusted with a suitable mechanism, can at the same time select a spectral component and focalize it, reducing the number of mirrors in the apparatus. In this paper, we present the mechanical configuration and the optical properties in the extreme ultraviolet of a low-cost active grating. The system has been tested in the 13-50 eV region, showing good optical properties and high efficiency, and the shape of the bent grating has been analyzed using a wavefront sensor. The proposed system could be used both in table-top experiments and in large scale facilities.

1. Introduction

High-order harmonic generation (HHG) in gases is a process widely used to generate extreme ultraviolet (XUV) and soft X ray pulses, both for large scale facilities [1,2] and table-top setups [3,4]. These pulses are polychromatic, consisting of multiple odd harmonics of the generating wavelength; most experiments, however, need only a specific spectral component, which can be extracted from the HHG light comb using a monochromator. The monochromatization of light can be achieved using two different optical components: multilayer mirrors and diffraction gratings. The second solution is usually preferred, especially when high spectral purity and tunability are required. In the widely used Czerny-Turner configuration, monochromatization is obtained using a planar diffraction grating, to select the spectral component, and two concave mirrors, to collimate and focalize the radiation. The grating introduces a pulse-front tilt, thus causing a temporal broadening of the selected pulses; a monochromator which does not compensate for this phenomenon is called non-compensated; conversely, a compensated monochromator is realized adding another grating and two more mirrors to the system, compensating for the pulse front tilt [5,6]. In some applications, the mirrors and the plane grating can be substituted by a single concave grating, namely a toroidal grating, able of both selecting and focalizing at the same time [7,8]. The grating has a fixed curvature radius, so it works in a fixed geometry, that is, fixed subtended angle and fixed arms. However, they are rather complex components to be realized. Another option is to use cylindrical gratings, which are much simpler and cheaper to produce than the toroidal gratings. Cylindrical gratings can be well suited in near grazing incidence condition [9], they are easier to manufacture, especially via hologram [10] and they are currently used to achieve ultrahigh resolution in the VUV range [11]. For example, the BL21B beamline at Taiwan Light Source (TLS) uses a cylindrical grating monochromator (U9-CGM) with 4 cylindrical gratings with different line density to achieve extremely high resolution in a

#562422 https://doi.org/10.1364/OE.562422
Journal © 2025 Received 18 Mar 2025; revised 14 May 2025; accepted 4 Jun 2025; published 7 Aug 2025

Optics EXPRESS

broadband energy range, from 5 to 100 eV [11]. In all these cases, the cylindrical grating is supposed to have fixed radius of curvature, thus working in fixed configuration.

The key idea of this work is to use a plane grating that is bent at different curvature radius to maintain the focus at different wavelengths when scanning the spectrum. Since the radius can be changed, the same grating can work in different geometries, i.e., different subtended angles and/or arms, depending on the requirements on the monochromator. Such an idea has been already tested in big-scale facilities such as the Dragon-type beamline at the National Synchrotron Radiation Research Center in Taiwan, aiming to eliminate the coma and defocus aberrations observed in a fixed-slit monochromator by using an active grating [12]. The proposed solution used a bulky grating with piezoelectric actuators which provided a deformation of the grating from the planar condition up to a radius of curvature of 40 m [13].

The research here presented aims to realize a much simpler device, a compact and low-cost mechanical design in which a planar grating is bent to different cylindrical shapes, thus becoming a concave grating, allowing the selection and focalization of different spectral components for table-top HHG setup. This paper follows previous work, increasing the readiness for the use in a beamline [14,15]. The radius of curvature is controlled by the operator and the overall setup reduces the number of optical elements involved, leading to simpler and cost-effective instrumentations. We designed and realized the suitable mechanism to bend a thin plane diffraction grating. We performed a characterization of the grating to assess the capabilities of spectral selection and light focalization. We also analyzed the wavefront shape to measure the shape of the grating during the bending process. We then performed a surface analysis to check the structural integrity of the grating surface after the bending operations.

2. Mechanical configuration

The planar diffraction grating used in our experiment is a replica of a mechanically ruled reflection grating, manufactured by Richardson Gratings. The replica is realized upon an annealed borosilicate crown glass (BK-7) substrate of 50×15 mm, 1.5 mm thick. The profile is replicated over an epoxy resin layer, gold coated to achieve high reflectivity in the XUV spectrum. The grating has a saw-tooth profile, with a blaze-angle of 1.6° and a ruling density of 246.16 grooves/mm.

The bending of the grating is obtained using the leverage principle [16]. The grating is glued onto two aluminum plates screwed to two bronze clamps, as shown in Fig. 1(a). One of the clamps is fixed to the aluminum base, while the other is free to move. The free clamp is moved via a Micronix linear actuator (micro pusher) which generates a bending moment onto the grating [12], as shown in Fig. 1(b). The glass substrate is able to bend up to a bending radius of about 2.7 m; in our tests, we never exceed a value of 3.20 m, remaining within the safety margin.

To evaluate the bending radius, we illuminate the grating with a He-Ne laser at a fixed angle of incidence and then we bend the grating until a Spiricon (mks Ophir) camera observed a focalized image. Since we use only a vertically ruled grating, we observe focalization only in the so-called tangential plane, i.e. horizontal. To reconstruct the curvature radius, we use Eq. (1):

$$\frac{1}{p} + \frac{1}{q} = \frac{2}{R \cos \alpha} \tag{1}$$

In Eq. (1), p is the input arm, i.e. the distance between the grating and the point source; q is the output arm, i.e. the distance between the grating and the focal plane; α is the incidence angle and R is bending radius of the grating. We fix p and α and we move the camera, used as beam profiler, at various focal plane positions q; the value of q is measured at the tangential focal plane, i.e. at the position in which the beam profile camera observed the narrowest possible image. We reconstruct the bending radius R with respect to the steps performed by the pusher, as shown in Fig. 2.

Optics EXPRESS

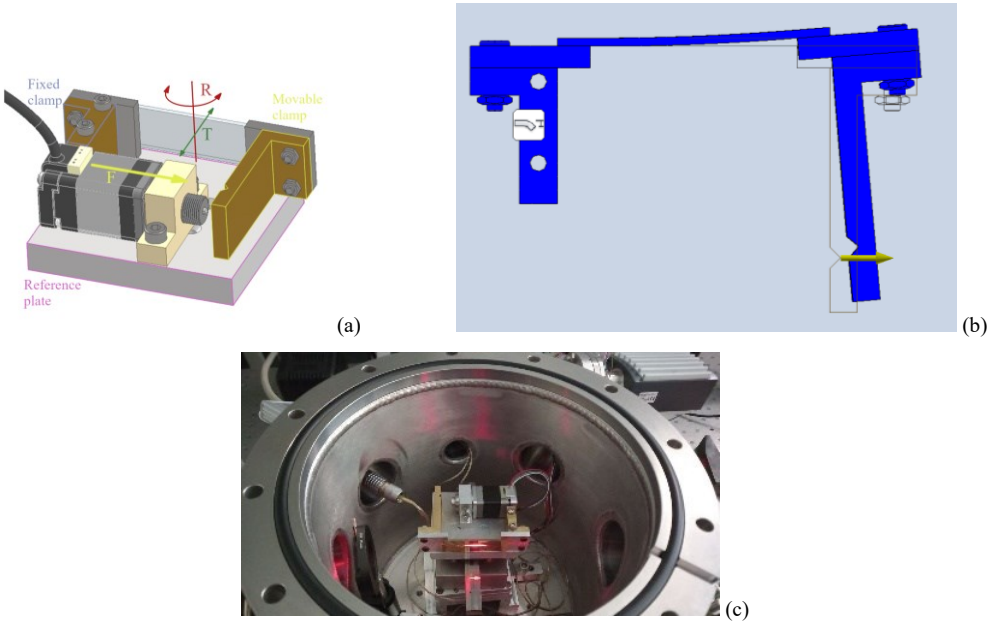

Fig. 1. (a) CAD model of the bendable grating assembly; (b) leverage principle applied to the grating; (c) mechanical assembly in the experimental chamber.

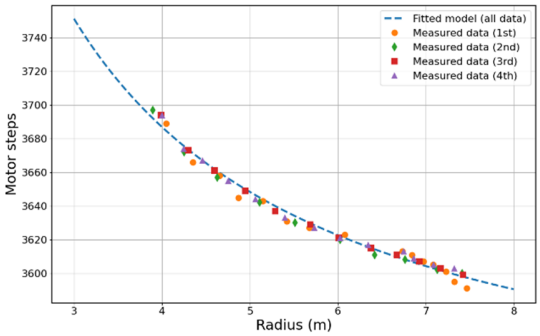

Fig. 2. Curvature radius *vs* motor steps.

Optics EXPRESS

We test the mechanical resistance of a grating by bending a glass substrate until the fracture of the glass substrate itself; such an event happened when the grating was maintained for several tens of minutes at curvature radius of about 2.7 m. Since in our test we never reached a curvature radius smaller than 3.2 m, we assume that the grating has never been in critical condition during the entire experiment. We also notice that the fracture happened at one of the glued edges and only after a certain time of accumulated stress, so it is possible that the grating could be momentarily bent at critical curvature radius without necessarily suffering a critical failure. The critical failure value is strongly dependent on the substrate material and the accuracy in the gluing process, so it must be considered as valid only within a certain type of experimental setup.

3. Spectral lines characterization methodology

To test the focusing properties of the bendable grating in the XUV, we prepared a vacuum experimental setup.

An XUV light source is placed at the end of the input arm p; an adjustable slit is placed just in front of the source, acting as the entrance slit of the spectroscopic system. A vacuum chamber contains an iris, to control the angular divergence of the XUV light, and the active grating with its bending mechanism (Fig. 1(c)). The grating is mounted onto two piezo actuators: a linear actuator to control the linear position of the grating and compensating for the pointing error (indicated with T in Fig. 1(a)), and a rotational stage to control the incidence angle and scan different wavelengths maintaining fixed both the input and output arms (indicated with R in Fig. 1(a)). The selected spectral component is directed into the output arm, in which an aluminum filter reduces the amount of stray visible light. The measurements are performed using a thermoelectrically cooled back-illuminated CCD (Princeton Instrument PIXIS 1300, 1340×1300, 20×20 µm pixel) placed at the end of the output arm. The entire system works as a constant-deviation monochromator, meaning that the deviation angle of the beam of light between the input and the output arms remained constant due to geometrical constraints. The grating itself, thanks to the rotating stage, changes its orientation allowing it to focalize different spectral lines. The geometry of the vacuum chamber allows a total deviation angle of 163°, with the input arm p and the output arm q both set at 700 mm. The entrance slit is regulated to a width of 100 µm; this width has been chosen since it is representative of the operational conditions of most of the monochromatic beamlines using high order harmonic sources. Inside the vacuum chamber, we place an iris with a diameter of 4 mm to control the angular opening of the XUV beam. The geometrical characteristics of the experimental setup are summarized in Table 1.

Table 1. Experimental setup characteristics

Experimental setup	
Input arm p	700 mm
Output arm q	700 mm
Deviation angle k	163°
Entrance slit aperture	100 µm × 5 mm
Entrance iris diameter	4 mm
Grating groove density σ	246.16 gr/mm

Diffraction and focusing properties of the bendable grating system follow Eq. (2):

$$\begin{cases} \frac{\cos^2\alpha}{p} + \frac{\cos^2\beta}{q} = \frac{\cos\alpha+\cos\beta}{R} \\ \sin\alpha - \sin\beta = m\sigma\lambda \\ \alpha + \beta = k \end{cases} \tag{2}$$

Optics EXPRESS

where α and β are the incidence angles between the normal of the grating and, respectively, the input and output arm; k is their sum and therefore the total deviation angle; m is the diffraction order; σ is the ruling density of the grating; λ is the observed wavelength and R is the radius of the grating. We can use the sum-to-product trigonometric formula to rewrite the second equation presented in Eq. (2) as:

$$2\sin\left(\frac{\alpha-\beta}{2}\right)\cos\left(\frac{\alpha+\beta}{2}\right)=m\sigma\lambda \tag{3}$$

Then, using the third equations presented in Eq. (2), we can write:

$$2\sin\left(\alpha-\frac{k}{2}\right)\cos\left(\frac{k}{2}\right)=m\sigma\lambda \tag{4}$$

Equation (4) relates the incidence angle α to the total deviation angle and to the wavelength of a specific diffracted order m. So, it is possible to select a specific spectral line by rotating the grating at the correct angle α and then to focalize it adjusting the grating radius of curvature using the micro-pusher.

The focusing test is performed using a hollow-cathode source (McPHERSON Model 629). We use two noble gases, helium and neon, observing two spectral lines for each gas, as described in Table 2.

Table 2. Observed spectral lines

Helium	Neon
30.3 nm (He II)	46.07-46.24 nm doublet (Ne II)
58.4 nm (He I)	73.5-74.3 nm doublet (Ne I)

During the experiment, the grating is illuminated by the XUV light and rotated until the spectral line is centered in the CCD. Then, several CCD images are taken, during a progressive bending of the grating. To ensure a sufficient level of bending and, at the same time, a well-spaced sampling, each image is taken after performing 5 steps with the pusher. From each image recorded with the CCD, a peak profile is extracted, summing the intensity value of each pixel along each column. This profile is used to measure the Full Width at Half Maximum, FWHM, that is used to assign the lateral dimension to the spot size, the FWHM being the width of the peak at half height. From the same profile, also the peak intensity is measured to assist during the identification of the focalized image. The curvature radius of the grating is computed for each sample using the *curvature radius vs motor steps* curve presented in Fig. 2. An example of the recorded images and of the extracted peak profile is presented in Fig. 3.

FWHM and peak intensity can be used together to identify the focalized image, thus identifying also the curvature radius corresponding to the best focusing condition. The FWHM is expressed in number of pixels and corresponds to the lateral dimension of the spectral line; the peak intensity is expressed in arbitrary unit (a.u.) corresponding to the intensity value as read by the acquiring software. Plotting both the FWHM and the intensity plot, it is possible to identify the curvature radius needed to obtain the focal position of the specific spectral line.

Optics EXPRESS

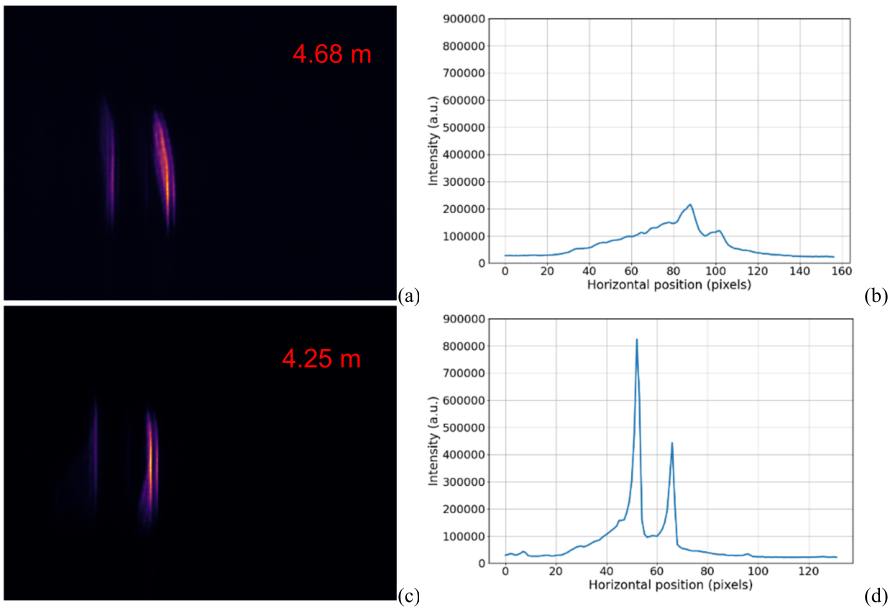

Fig. 3. CCD images of spectral lines of Ne I doublet centered at 46.1 nm and one-dimensional peak profile of the images, taken with two radii of curvature: (a) and (b), 4.68 m (out of focus); (c) and (d), 3.45 m (in focus).

4. Spectral lines characterization

The McPHERSON Model 629 Hollow Cathode Light Source is a gas discharge source with a water-cooling system. It operated at 450 V with a current of 100 mA. The pressure of both helium and neon was set at $4 \cdot 10^{-1}$ $mbar$. Also in this case, the CCD camera was cooled down to -20°C to reduce the thermal noise and an acquisition time of 10 s was set. The images were binned using a binning ratio of 2:1.

We observe an average FWHM of 4.25 pixels for the helium lines at 30.3 nm and 58.4 nm (Fig. 4), corresponding to 85 µm, while the two neon doublets had larger FWHM, 5 pixels for the doublet centered at 46.1 nm (Fig. 5(a)), corresponding to 100 µm, and roughly 15 pixels (160 µm) for the doublet centered at 74.0 nm (Fig. 5(b)). The worst focusing at the Ne doublet centered at 74.0 nm is due to the fact that the spectral distance between the two lines is approaching the spectral resolution, that is mainly limited by the width of the entrance aperture (100 µm slit).

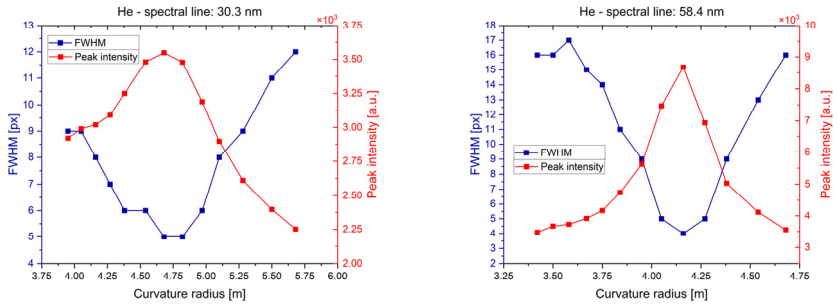

Fig. 4. Helium focusing curves. (a): 30.3 nm; (b) 58.4 nm.

Optics EXPRESS

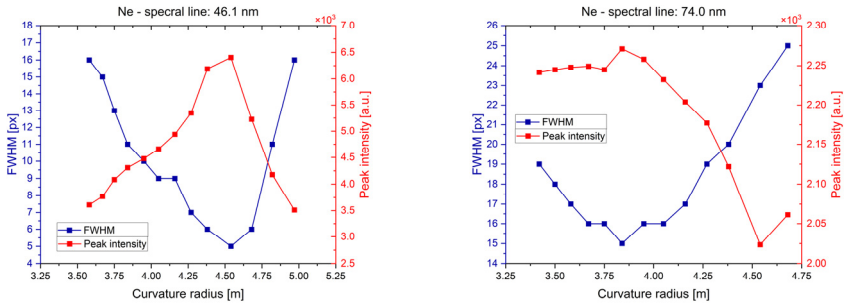

(a) (b)

Fig. 5. Neon focusing curves. (a): 46.1 nm; (b) 74.0 nm.

5. XUV measured and theoretical data comparison

Table 3 summarizes the measured data, in terms of both incidence angle and curvature radius corresponding to the focalized image. The data are compared to the theoretical value for both the incidence angle and the curvature radius that can be obtained using the equation of the grating.

Table 3. Measured and theoretical curvature radii

		Measured data		Theoretical data	
gas	λ (nm)	α (°)	R (m)	α (°)	R (m)
He	30.3	82.5	4.68	82.95	4.61
	58.4	84.45	4.16	84.29	4.29
Ne	46.1	83.6	4.54	83.70	4.45
	74.0	84.9	3.84	85.03	4.05

We observed small differences between the measured set of curvature radius and the theoretical one. However, using the *curvature radius vs motor step* shown in Fig. 2, we found that such differences are always in the range of ± 5 motor steps, thus meaning that the difference is always smaller than our sampling frequency.

Observing both the Figs. from 4 and 5 and Table 3, we noticed that the FWHM focalization curves have a clear minimum, with almost no possibilities of misinterpretation. The minimum of the FWHM curve is also always aligned with the maximum of the intensity curve. These measurements highlight the capabilities of the active grating to correctly select and focalize different spectral components.

6. Grating efficiency

We analyzed the diffraction efficiency of the grating at the circular polarization–CiPo [17] beamline at Elettra Sincrotrone Trieste. The beamline allows to select different input energies with different polarization. Using a combination of undulators and gratings, we selected several energies in a spectral range from 20 to 40 eV (62 to 31 nm), at both vertical and horizontal polarization. The experiment is divided into two phases. First, we measured the intensity of CiPo light at the different energies on the CCD camera. The camera was placed 700 mm from the beamline focus; at each energy, the working parameters of the beamline in terms of slit apertures and undulators parameters were recorded in order to replicate the working conditions in the second phase. Also, an AXUV100G photodiode by OPTO DIODE was inserted just before the CCD camera to measure the light intensity and the beamline stability.

Optics EXPRESS

In the second phase, we inserted the vacuum chamber with the bendable grating at 700 mm from the beamline focus and the CCD camera was placed at 700 mm from the grating, thus replicating the same geometrical and optical setup already tested in our laboratory. We replicated the same experimental conditions, in terms of energy, slit apertures and undulators parameters and we also measured the intensity of the light using the photodiode. The photodiode was necessary in order to consider the possible instability of the beamline, which could modify the intensity of the light and thus make impossible to perform a comparison between the measurements taken in the two different phases. We rotated the bendable grating to select the first diffraction order and we recorded the intensity of the first diffracted signal on the CCD.

The ratio between the direct measurements taken in the first phase and the measurements of the first diffracted order taken in the second phase gives the diffraction efficiency of the grating. The results are shown in Fig. 6.

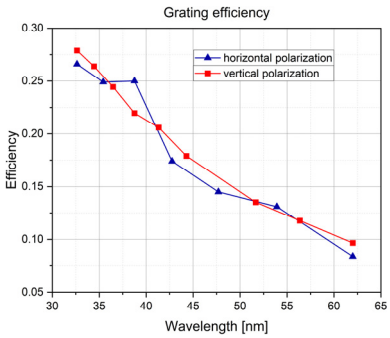

Fig. 6. Diffraction efficiency of the grating.

The diffraction efficiency shows a monotone growth from low energy to high energy. The diffraction efficiency decreases from >25% at 32 nm to 9% at 61 nm. We observe slightly higher efficiency for the vertically polarized beam, i.e., s-polarized light. The efficiency measured is comparable to the efficiency measured for similar replica gratings in the same classical diffraction mount configuration [18,19].

7. Wavefront characterization

We performed an analysis of the grating surface shape using a wavefront sensor. The idea was to measure the aberrations of the wavefront and then reconstruct the real shape of the bendable grating, to understand if the bending was actually creating a cylindrical shape and then which were the types of aberrations introduced. We used a technique applied typically to adaptive optics: the surface under test was illuminated with a plane wavefront, a wavefront sensor (WFS) measured the wavefront phase of the reflected light and then, by using the Zernike polynomials, it was possible to reconstruct the true shape of the surface [20].

We used a typical Shack-Hartmann WFS, which can measure the wavefront shape by measuring its local gradients. An array of lenslets performed the sampling of the wavefront and focused each portion of the beam of light on the sensor of a CMOS camera separately. The experimental setup was composed of a laser diode (Thorlabs CPS670, λ = 670 nm, power 4.5 mW) whose light was collimated by a set of lenses. A beam splitter divided the incoming light beam into two portions, one directed towards the grating and the other reduced by a telescope and directed to the WFS camera. A plane mirror was used as reference mirror: the surface was considered perfectly plane and we used it to validate and calibrate the setup, see Fig. 7. The bendable grating is illuminated in its middle portion with a circular beam of 9 mm in diameter, which meant that

Optics EXPRESS

the grating was scanned for its shape only in its center, but this fact was acceptable since the grating was effectively using only its middle portion to focus the XUV light.

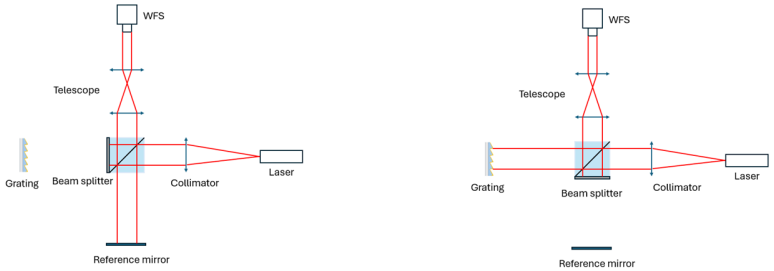

Fig. 7. Setup for the wavefront analysis, with the measurement of the reference mirror (a) and of the bendable grating (b).

The WFS camera was a USB 3.0 global shutter CMOS monochromatic sensor with 5.86 µm square pixel, produced by *iDS* (UI-3060CP-M-GL Rev.2). The lenslet array was composed by lenslet of $L = 150$ µm with a focal length of $f = 6.4$ mm. The area observed was 24×24 pixel and the spot images were converted in 8-bit integer matrices representing the quantized pixel intensity.

The grating was bent from a plane configuration (i.e., radius of curvature equal to infinity) up to 5 m; for each one of the 11 measurements, the reconstructed slope was fitted with the Zernike polynomials and the coefficients were then plotted against the radius of curvature, in order to understand which aberrations were induced by the bending process. Figure 8 shows the reconstructed surface of the grating.

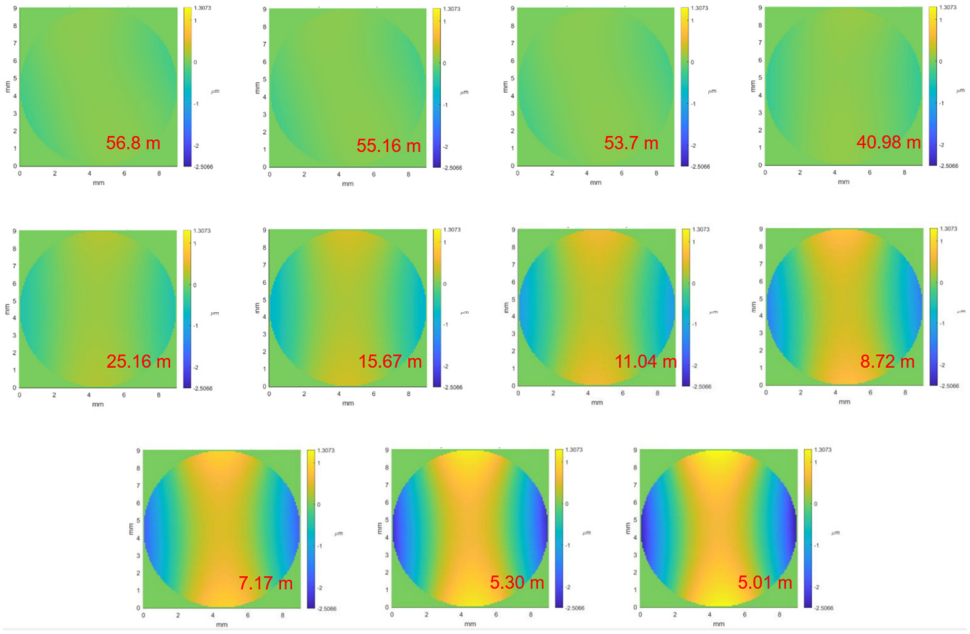

Fig. 8. Reconstructed surface of the illuminated portion of the grating, for decreasing radius of curvature.

Optics EXPRESS

In Fig. 9(a) we plotted the coefficients linked to the three principal aberrations: the tangential astigmatism (Astigmatism X), the sagittal astigmatism (Astigmatism Y) and the defocus; values are in fraction of wavelength λ of aberration.

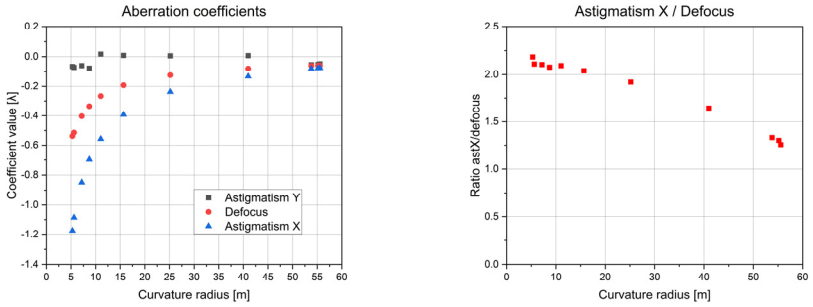

(a) (b)

Fig. 9. (a) Zernike coefficients, for decreasing radius of curvature; (b) ratio between astigmatism X and defocus.

Plotted against the radius of curvature, we observed that the aberrations were close to zero for high value of curvature radius (plane grating condition), while their magnitudes increased as the radius of curvature decreases (bent grating condition). In particular, tangential astigmatism and defocus both increased, as we expected since the grating was deformed into a cylindrical shape. The ratio between the two aberrations tends to be a constant value as the radius of curvature decreased, coherently with the supposed cylindric shape of the wavefront. In fact, a constant ratio value of $\sqrt{2}$ between the tangential astigmatism and the defocus described a perfect cylindrical wavefront, and so a grating bent to the same cylindrical shape [21]. In our case, as shown in Fig. 9(b), the constant value is close to 2.1, so the grating is bent to a non-perfect cylindrical shape. The most probable cause of this effect has to be researched in an unwanted torsional deformation induced during the bending. Such torsional deformation can produce a variation in the ratio between the tangential astigmatism and the defocus and can also induce a small sagittal astigmatism. The torsional deformation can be induced by a small off-pointing of the pusher tip with respect to the V-shaped rail of the movable bronze arm (see Fig. 1(a)) or by a non-uniformity of the thickness of the glue between the grating and the two aluminum plates. In both cases, an off-centered and asymmetrical force was induced during the bending, leading to the generation of a torsional moment onto the grating itself. Considering that both the mounting and the gluing of the bendable grating were realized by hand, small defects in the overall configuration must be expected, although these errors do not compromise the results of the experiment in terms of spectral lines selection and focusing. However, we must consider that the height of the illuminated area when working at grazing incidence is much smaller than the width of the area itself (being amplified by the factor $\cos(\alpha)^{-1}$), typically few millimeters against a couple of centimeters. The sagittal astigmatism was analyzed on an extension of 9 mm, if we limit the analysis to the practical case of ≈3 mm (in height) the value is much lower.

The sagittal astigmatism (Astigmatism Y) is an unwanted aberration, since it is directly connected to a deformation not related to the pure cylindrical one that we wanted. The probable cause of this sagittal astigmatism is the same torsional deformation already described. The value of sagittal astigmatism was close to zero, so its effects on the performance were negligible.

The wavefront analysis shows that the grating was bent in a cylindrical shape with small deviation from an ideal cylindrical shape due probably to some non-uniformity during the gluing process; the sagittal astigmatism is quite negligible.

Optics EXPRESS

8. Surface analysis

We analyzed the diffraction grating surface using an optical microscope and an Atomic Force Microscope (AFM) to reconstruct the actual surface profile and to verify the characteristics of the surface. We measured the grating two times: one before gluing it on the two small plates, and the second one after an entire cycle of measurements. In this way, we were able to verify if the gluing process and/or the bending of the grating has produced any damage to the grating surface. Our main concern was related to the possibility that the stress induced by the bending process might have damaged the coating of the grating, causing cracks in the resin or partial detachment of the gold coating. The optical microscopy allows us to find visible damage onto the surface, such as scratches and marks, while the AFM analysis can highlight extremely small features (fractions of nm), allowing to analyze the microroughness of the surface.

Using the optical microscope, we observed no visible scratches or marks on the surface of the gratings (see Fig. 10); the optical microscope showed only some dust particles deposited onto the surface, a foreseen and expected event due to the handling, since we had to unscrew the grating from the mechanism and then move it from the vacuum chamber to the optical microscope location.

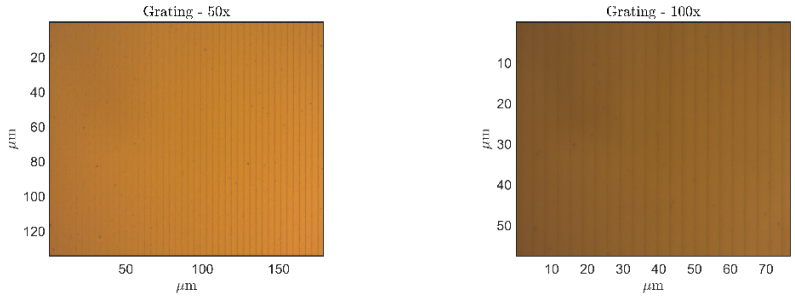

(a) (b)

Fig. 10. Optical microscope images: no scratches or marks were observed. (a) zoom 50; (b) zoom 100.

With the AFM we measure an area of 20 µm × 20 µm, positioned roughly at the center of the grating. We observed that the only visible difference is the amount of dust grains deposited onto the surface before and after the test (see Fig. 11). No defects have been observed, and the coating appears undamaged by the bending tests.

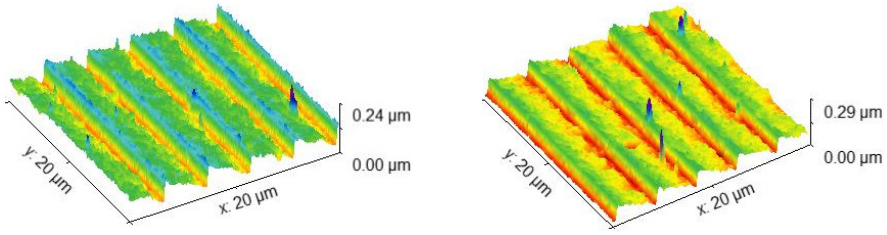

(a) (b)

Fig. 11. AFM images: (a) before the test campaign, (b) after the test campaign.

From the 2-D acquired plot (Fig. 12(a)) we extract a 1-D profile of the grating surface (Fig. 12(b)) to evaluate the precision of manufacturing. The plot shows that the distance between two peaks or two valleys is on average equal to 4.07 μm; the theoretical distance, obtained

Optics EXPRESS

calculating the inverse of the ruling density of 246.16 *grooves/mm,* is 4.062 μ*m*. Considering the manufacturing and the measurement errors, we conclude that the grating has the declared ruling density.

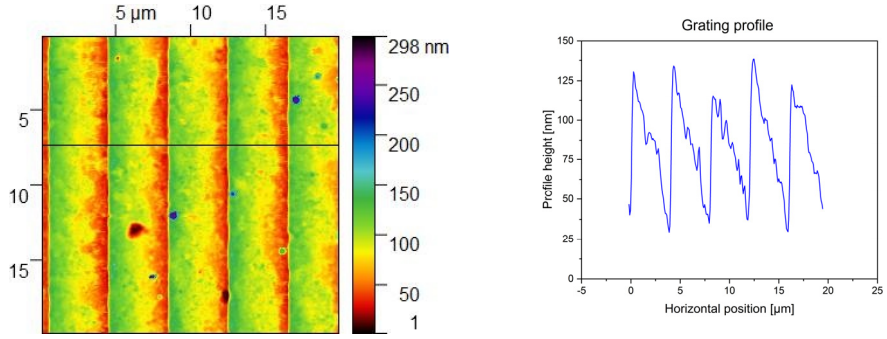

(a) (b)

Fig. 12. (a) Pseudocolor image of the grating surface; (b) Profile of the grating corresponding to the black line on the panel (a).

We use linear fit to simulate the ideal sawtooth profile (Fig. 13(a)). Then, we subtract the linear fit values from the actual data, obtaining the roughness profile (Fig. 13(b)). From the roughness profile we calculated two main parameters: the average roughness R_a and the root-mean-square roughness R_q [22], using Eq. (5) and (6):

$$R_a = \frac{1}{l}\int_0^l |z(x)|dx \tag{5}$$

$$R_q = \sqrt{\frac{1}{l}\int_0^l z(x)^2 dx} \tag{6}$$

where l is the total length of the analyzed section and $z(x)$ is the roughness profile. We measure a $R_a = 3.88\ nm$ and a $R_q = 5.60\ nm$.

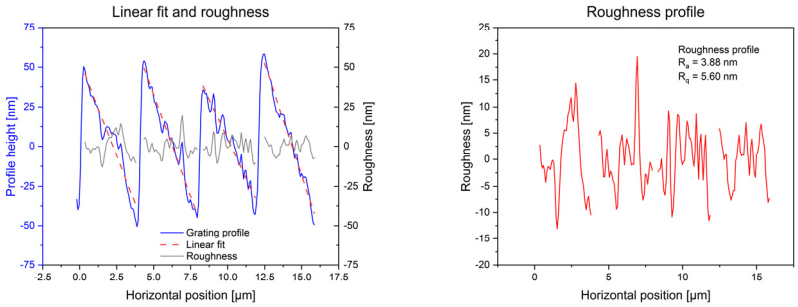

(a) (b)

Fig. 13. (a) Linear fit of the grating profile; (b) Roughness profile obtained subtracting the fitting model from the measured data.

From the extracted profile we also evaluate the blaze angle of the grating. We measure the total height of each groove and its width, then we calculate the blaze angle of each groove. The average blaze angle measured is 1.54°, which is very close to the declared blaze angle 1.6°; the main contributor to this small variation is the truncated apex of the third groove.

Optics EXPRESS

9. Conclusions

In our study we analyzed the properties of a bendable grating to be used for the realization of compact extreme-ultraviolet monochromators, particularly for table-top beamlines such those dedicated to high-order laser harmonics. The optical and the spectral properties of a thin replica plane grating bent from plane to few-meters radius have been tested. The results show that such an optical element has performance suitable for the simultaneous monochromatization and focalization of XUV spectral component.

The spectral line characterization has shown the capabilities of the bendable grating in the selection and the focalization of different spectral lines; the results show that the grating can focalize with very good accuracy along the tangential (horizontal) plane different spectral lines and the system is also able to resolve even close spaced doublets. The comparison with the simulated experiment shows that the actual behavior of the mechanical system is close to the theoretical one and the results can be considered validated also by the theory.

The efficiency analysis shows that the grating has a good diffraction efficiency at the first diffraction order, compatible with the characteristics of the replica grating.

The wavefront analysis allows us to assess the actual shape of the grating after the bending; we observed that the mechanism in fact produces quite perfect cylindrical shape, with little unwanted aberration (sagittal astigmatism), very reduced for small curvature radius.

The optical and atomic force microscopic analysis have proven that no damages of the reflective surface have been produced by the bending process; the AFM analysis has also measured the surface roughness, revealing that the low-cost grating has a limited surface roughness.

The use of bendable gratings is very useful in simplifying the optical design of table-top beamlines, since it helps in minimizing the number of required optical elements for the realization of a full beamline. In the case of a monochromatic beamline with a single-grating design, just two optical elements are required: the bendable grating with its exit slit and the refocusing toroidal mirror to give the final focus on the sample. A time-delay-compensated beamline, where two diffractive elements are required, could be realized with three optical elements, as already discussed in Ref. [11]: 1) the first grating with its exit slit to perform the spectral selection; 2) the second grating which compensates for the pulse-front tilt and gives the horizontal focus on the sample; and 3) a cylindrical mirror to give the vertical focus on the sample. The number of optical elements is substantially reduced with respect to the design using plane gratings [5]. Furthermore, the use of a replica plane grating bent in various cylindrical shapes is an extremely cost-effective solution with respect to a variable space line (VLS) plane grating and to a spherical grating, making our system an interesting solution for table-top setup with limited budget available.

Potential future developments of this device could be the realization of a two stages system, with a cylindrical mirror and another bendable grating, realizing a complete beamline using the capabilities of the tested bendable grating.

Funding. Ministero dell'Università e della Ricerca (PRR.AP026.016); National Recovery and Resilience Plan (B53C22001750006); Italian Ministry of University and Research (EUROFEL-ROADMAP ESFRI).

Acknowledgments. The development activities at the CNR Institute for Photonics and Nanotechnologies in Padova have been performed in the framework of the I-PHOQS facility, Activity 3.1: Optics for ultraintense and ultrashort beams (Integrated Infrastructure Initiative In Photonic and Quantum Sciences (PRR.AP026.016-CUP B53C22001750006)), funded by the National Recovery and Resilience Plan. For the measurements done at CIPO, the authors acknowledge funding through the project EUROFEL-ROADMAP ESFRI of the Italian Ministry of University and Research. LP acknowledges the partial contribution from the project NEST - Network for Energy Sustainable Transition (CUP: B53C22004060006).

Disclosures. The authors declare no conflicts of interest.

Data availability. Data underlying the results presented in this paper are not publicly available at this time but may be obtained from the authors upon reasonable request.

References

Optics EXPRESS

1. M. Labat, O. Tcherbakoff, G. Lambert, *et al.*, "Test of HHG chambers for seeding at SPARC," NIM-A **593**(1-2), 26–29 (2008).
2. C. Chiang, M. Huth, A. Trützschler, *et al.*, "Efficient and tunable high-order harmonic light sources for photoelectron spectroscopy at surfaces," J. Electron Spectrosc. Relat. Phenom. **200**, 15–21 (2015).
3. L. Barreau, A. D. Ross, S. Garg, *et al.*, "Efficient table-top dual-wavelength beamline for ultrafast transient absorption spectroscopy in the soft X-ray region," Sci. Rep. **10**(1), 5773 (2020).
4. M. Kretschmar, M. J. J. Vrakking, and B. Schutte, "Intense XUV pulses from a compact HGG setup using a single harmonic," J. Phys. B: At. Mol. Opt. Phys. **54**(20), 20LT01 (2021).
5. L. Poletto and F. Frassetto, "Time-preserving grating monochromators for ultrafast extreme-ultraviolet pulses," Appl. Opt. **49**(28), 5465 (2010).
6. L. Poletto and F. Frassetto, "Temporal response of ultrafast grating monochromators," Appl. Sci. **8**(1), 5–9 (2017).
7. M. Ito, Y. Kataoka, T. Okamoto, *et al.*, "Spatiotemporal characterization of single-order high harmonic pulses from time-compensated toroidal-grating monochromator," Opt. Express **18**(6), 6071–6078 (2010).
8. H. Igarashi, A. Makida, M. Ito, *et al.*, "Pulse compression of phase-matched high harmonic pulses from a time-delay compensated monochromator," Opt. Express **20**(4), 3725–3732 (2012).
9. B. E. Woodgate, "Cylindrical and spherical gratings," J. Opt. Soc. Am. **64**(5), 654–661 (1974).
10. X. Lin, "The Dispersive Properties of Cylindrical Concave Grating and its Application," High Power Laser and Particle Beam **12**(4), 471–475 (2000).
11. Y. F. Song, J.-Y. Yuh, Y.-Y. Lee, *et al.*, "Performance of an ultrahigh resolution cylindrical grating monochromator undulator beamline," Rev. Sci. Instrum. **77**(8), 085102 (2006).
12. H. S. Fung, C. T. Chen, L. J. Huang, *et al.*, "A Novel Active Grating Monochromator - Active Grating Spectrometer Beamline System for Inelastic Soft-X-ray Scattering Experiments," AIP Conf. Proc. **705**, 655–658 (2004).
13. H. S. Fung, J. Y. Yuh, L. J. Huang, *et al.*, "A Soft X-Ray (300-1000 eV) Active Grating Monochromator Beamline at NSRRC," AIP Conf. Proc. **879**, 563–566 (2007).
14. F. Frassetto, S. Bonora, C. Vozzi, *et al.*, "Active-grating monochromator for the spectral selection of ultrashort pulses," Opt. Express **21**(11), 12996–13004 (2013).
15. F. Samparisi, F. Frassetto, G. Zeni, *et al.*, "Realization of a cost-effective deformable grating for extreme ultraviolet," J. Phys.: Conf. Ser. **2380**(1), 012058 (2022).
16. M. Vannoni, I. Freijo Martin, and H. Sinn, "Characterization of an X-ray mirror mechanical bender for the European XFEL," J. Synchrotron Radiat. **23**(4), 855–860 (2016).
17. A. Derossi, F. Lama, M. Piacentini, *et al.*, "High flux and high resolution beamline for elliptically polarized radiation in the vacuum ultraviolet and soft x-ray regions," Rev. Sci. Instrum. **66**(2), 1718–1720 (1995).
18. N. Fabris, F. Frassetto, P. Miotti, *et al.*, "Comparison between classical and off-plane diffraction efficiency for the soft X-ray region," *SPIE Proc.* 11038, X-Ray Free-Electron Lasers: Advances in Source Development and Instrumentation, 11038OW (2019).
19. P. Miotti, N. Fabris, F. Frassetto, *et al.*, "Design and realization of a XUV plane-grating monochromator at variable included angle," *SPIE Proc.* 10760, Advances in X-Ray/EUV Optics and Components XIII, 1076009 (2018).
20. R. G. Lane and M. Tallon, "Wave-front reconstruction using a Shack–Hartmann sensor," Appl. Opt. **31**(32), 6902–6908 (1992).
21. J. C. Wyant and K. Creath, "Basic Wavefront Aberration Theory for Optical Metrology," Applied Optics and Optical Engineering XI, (1992).
22. D. Whitehouse, *Surfaces and their Measurements*, Hermes Penton Science, Taylor Hobson Ltd (2002).